

Sparsity is All You Need: Improved Coding with Selective Sensing

Yizhou Lu

*Department of Electrical
and Computer Engineering
University of Wisconsin-Madison
Madison, Wisconsin 53706
Email: ylu289@wisc.edu*

Trevor Seets

*Department of Electrical
and Computer Engineering
University of Wisconsin-Madison
Madison, Wisconsin 53706
Email: seets@wisc.edu*

Ehsan Ahmadi

*Department of Electrical
and Computer Engineering
University of Wisconsin-Madison
Madison, Wisconsin 53706
Email: eahmadi2@wisc.edu*

Felipe Gutierrez-Barragan

*Department of Computer Sciences
University of Wisconsin-Madison
Madison, Wisconsin 53706
Email: fgutierrez3@wisc.edu*

Andreas Velten

*Department of Biostatistics and Medical Informatics
Department of Electrical and Computer Engineering
University of Wisconsin-Madison
Madison, Wisconsin 53706
Email: velten@wisc.edu*

Abstract—

Optical coding has been widely adopted to improve the imaging techniques. Traditional coding strategies developed under additive Gaussian noise fail to perform optimally in the presence of Poisson noise. It has been observed in previous studies that coding performance varies significantly between these two noise models. In this work, we introduce a novel approach called selective sensing, which leverages training data to learn priors and optimizes the coding strategies for downstream classification tasks. By adapting to the specific characteristics of photon-counting sensors, the proposed method aims to improve coding performance under Poisson noise and enhance overall classification accuracy. Experimental and simulated results demonstrate the effectiveness of selective sensing in comparison to traditional coding strategies, highlighting its potential for practical applications in photon counting scenarios where Poisson noise are prevalent.

1. Introduction

An imaging device performs a projection from a high-dimensional scene space onto a lower-dimensional reconstruction space. The need for the projection stems partially from a need to reduce and interpret the data, either as a human-interpretable image or as some form of pattern yielding actionable information about the scene. In addition, especially when imaging with visible light, a projection reduces the information to an amount that can be digitized by a camera sensor and processed. Camera sensors are two-dimensional and capture the absolute value squared of the light wave averaged over pixels in space, time, wavelength, and polarization. The projection onto a sensor prior to digitization is thus a fundamental and essential component of any imaging and vision device for physical and computational

reasons. One quite general way to model this projection process is through what is commonly referred to as coding or multiplexing.

Mathematically, coding, it can be described as a linear operator, \mathbf{M} linking a vectorized incoming light field \mathbf{x} to a vector of light measurements \mathbf{y} . The **single-pixel-imaging** is considered as a typical example. Supposing the image of the field of view consists of $N \in \mathbb{Z}^+$ pixels and is measured by $m \in \mathbb{Z}^+$ projections, the single-pixel-sensing process, if ignoring noise, can be expressed as the following equation

$$\mathbf{y} = \mathbf{M}\mathbf{x} \quad (1)$$

, where $\mathbf{x} \in \mathbb{R}^{N \times 1}$ is the image representation of the field of view, $\mathbf{M} \in \mathbb{R}^{m \times N}$ is a set of sensing masks linearly projecting the field of view onto the sensor pixels, and $\mathbf{y} \in \mathbb{R}^{m \times 1}$ are the corresponding measured flux levels or photon counts [1]. Physically, \mathbf{M} can be implemented by directing or blocking different parts of the incoming light with masks [2] and averaging them on sensors that digitize the detected flux levels or photon counts.

A linear operator with a mask can model most optics, including a lens that forms an image, color filters that provide color resolution, and camera pixels that average incoming light over an exposure time. The digitized vector then is processed computationally to extract the desired information about the scene. For a full rank measurement \mathbf{M} , a linear operation \mathbf{M}^{-1} can in principle allow reconstruction of the entire incoming measurement. In the simplest case, where the desired information is directly digitized, \mathbf{M} is a diagonal matrix. However far more elaborate capture and post-processing are being employed and are the basis of diverse fields such as structured illumination imaging, computational imaging (CI) [3] and compressed sensing. The primary benefits of complex codes are the improved signal to noise ratio do to the fact that the corresponding masks transmit more light, as well as the possibility of using

[§] Andreas Velten is corresponding author.

fewer masks and thereby reducing the overall complexity of the measurement.

Coding schemes have been extensively studied, but usually based on low noise scenarios or Additive Gaussian noise (AGN) models. AGN is a linear noise model that allows for rigorous mathematical treatment. It is a good model for the readout and background noise introduced by imperfect measurement hardware of past cameras and sensors. However, with the advancement of optical imaging and single photon sensitive sensor technologies, readout noise is decreasing, and Poisson noise is becoming dominant in measured imaging data. While the readout noise level of consumer cameras is approaching single electron levels, many state-of-the-art and emerging sensors technologies, such as Single-photon Avalanche Diode (SPAD), Quanta Image Sensors (QiS), and qCMOS cameras, directly measure quantized photon counts and as a result only experience Poisson noise [4], [5], [6].

Poisson noise is a fundamental physical property of light and arises from the discrete nature of light measurements. It is impossible to spread out a photon measurement over all the open pixels in a mask as the linear model introduced in Equation 1 assumes. The measurements of y that equation calls for are therefore impossible. Unfortunately, this has the consequence that the coding and thereby compressed sensing approaches designed to be effective under AGN or noiseless conditions are not effective under Poisson noise and their use is discouraged in the literature [1], [7], [8].

In this project, we use the popular a single pixel camera design to analyze and design effective coding models under Poisson noise. Similar to the conclusion of Cossairt et al., Harwid et. al., and Swift et. al., and Willett et. al. we find that general prior free coding provides no benefit over a trivial raster scanning approach using a diagonal matrix M [1], [3], [7], [8], [9], [10], [11], [12], [13]. We find, however, that in applications like compressed sensing and pattern recognition, where the collected data is compressible, similar benefits to those seen in compressed sensing and computational imaging can be seen if appropriate adjustments to the measurement matrices are made. We propose a coding methodology called **Selective Sensing** (SS) that relies on finding codes in basis where the signal is sparse and compressible to be used at capture time. This approach proves particularly effective for extremely sparse and compressible signals such as character recognition, as it enables the retention of key information while reducing the impact of noise on downstream analyses.

Our contributions are as listed.

- We analyze the performance of coding techniques using toy applications in single-pixel-imaging, compare the behavior of popular approaches for both additive Gaussian and Poisson noise, and develop coding strategies that work under Poisson noise.
- We find that coding can provide significant performance gains *only* when codes used in hardware capture are optimized specifically for downstream image reconstruction or vision tasks, such as classification.
- We propose the concept of selective sensing (SS) which includes coding methods selectively extract the features

directly for downstream tasks.

- We provide a method to create masks optimized for Poisson noise using a neural network.

2. Related Work

Coding under Poisson noise. In single-pixel imaging, coding allows the capture of a two-dimensional image with a single-pixel sensor [7]. Hadamard matrices are considered the optimal coding scheme for multiplexing [3], [7], [10] in systems with only additive gaussian noise. However, when Poisson noise is predominant, we should not use any coding [3], [7]. When the noise is Poisson distributed, coding with sparse priors such as compresses sensing are not recommended [1], [14].

End-to-end optimization This method refers to training hardware and software networks for image processing pipelines [15], [16]. In many previous projects, this idea was usually implemented without considering Poisson noise [17], [18], [19], [20], [21], [22] or without optimizing masks under Poisson noise during training [15], [23], [24], [25], [26]. Rego et. al froze the sensing matrix as a pinhole without optimizing it [24] Wang et al. [26] successfully implemented a neural network model for handwritten number classification on an optical device with limited photon budget, demonstrating the potential for AI-assisted optimization of coding schemes in CI. However, the Poisson noise was considered only in model testing where the most robust model was picked from a set of hyper-parameter combinations [26]. Our contribution is developing a noise-included training approach within a neural network model to find the optimal masks under Poisson noise.

3. Background

Our study on coding focuses on the single pixel camera, which serves as a specific implementation that provides a well-studied example of coding. We use this system as a toy model to investigate the problem, but our findings have broader implications and can be generalized to any form of coding.

3.1. Model Formulation

Recall the model described by Equation 1. The sensing matrix M can be generated using either computational or non-computational imaging methods. The key difference between the two is that computational imaging involves additional steps of optical coding and computational decoding to capture and process the image [3], while non-computational method, i.e. Raster scan, , involves measuring each pixel sequentially [25]. In the case of Raster scan, $M = I$, which is an identity matrix. In contrast, computational methods measure a combination of pixels simultaneously and can be further classified based on the type of masks used. For example, Hadamard matrices composed of ± 1 have been shown to be the optimal coding strategy for reconstruction

under the AGN [7]. A useful feature of computational methods is their compressibility. If the signal is sparse in the subspace of M , it is likely that only a few vectors of M are needed.

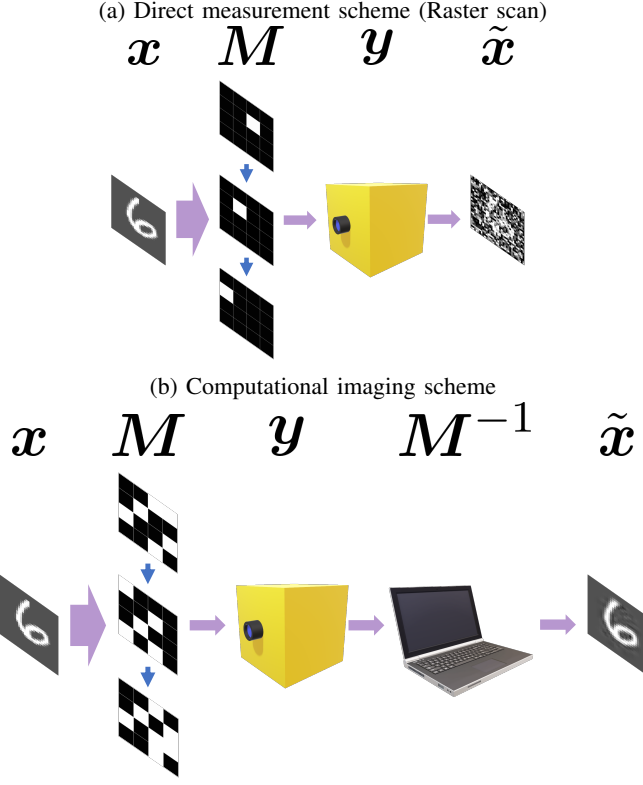


Figure 1: Single-Pixel imaging methods. x : object, M : masks of coding, y : counted photon numbers at the sensor, M^{-1} : reconstruction operator, \tilde{x} : reconstructed object. (a) Only one pixel (white) is scanned in each measurement, and the measured data requires no reconstruction. (b) The sum of all white pixels is measured in each measurement and it requires a decoding step to reconstruct the field of view.

In this paper, our main objective is to identify the optimal coding strategy among various commonly used methods. However, we face two fundamental physical constraints when implementing the coding strategy optically, as expressed by Equation 1 [1], [27].

- 1) **Flux-preserving** [1]. The single-pixel imaging model involves the allocation of available photons among masks, as discussed in [27]. It is important to ensure that the mask basis M does not produce additional photons through improper entries [27]. Mathematically, $\sup \sum_{i=1}^m M_{ij} = 1, \forall j \in \{1, 2, \dots, N\}$ [27].
- 2) **Positivity-preserving** [1]. It is not possible to physically implement negative values for the masks M , as demonstrated in [1], [27].

3.2. Model under Noise

This project investigates two noise models. The first one is the additive Gaussian noise (AGN) or read noise, which mainly originates from thermal vibrations of atoms at sensors. In this noise model, Equation 1 becomes:

$$\tilde{y} = Mx + \epsilon \quad (2)$$

, where $\epsilon \sim \mathcal{N}(\mathbf{0}, \sigma^2 I)$, and σ is the standard deviation. The other noise model is the Poisson noise or shot noise, which arises from the statistical nature of photons [28]. The measurement equation for this noise model is:

$$\tilde{y} \sim \mathcal{P}(Mx) \quad (3)$$

. It should be noted that the constraint 2 in Equation 3 prohibits negative entries in M .

4. Methods

4.1. Model Configuration

All coding strategies for classification tasks share the same fundamental model structure, as illustrated in figure 2. To classify handwritten numbers using optical devices with limited photon budget, we built a PyTorch-based pipeline consisting of a *scanner* module and a *classifier* module. The scanner module simulates the photon counting process using the techniques described in section 3.1. For the classification task, we utilized a two-hidden layer artificial neural network (ANN) with 40 and 128 nodes, serving as the primary model. To prevent overfitting and enhance generalizability, we applied dropout after each hidden layer, followed by a rectified linear unit (ReLU) activation layer.

During the training of the model, the scanner computes the photon counts with noise and then transmits this data to the classifier. The noise is sampled from a pre-defined noise distribution and varies across epochs. Once the loss has been computed, gradient descent is used to optimize the parameters of the classifier. **What sets the ONN apart from other models is that back-propagation is extended into the scanner, allowing for the simultaneous optimization of the masks and the classifier under different noise models.** This approach offers distinct advantages compared to traditional methods, which typically optimize the classifier independently of the scanner or optimize the scanner without the appropriate noise model.

ONN can also be used for reconstruction. To address this, we propose a simple approach of optimizing the ONN masks for a reconstruction task under different noise models. To achieve this, we developed a new ONN model with $m = N$ masks. The scanner takes raw image vectors x and outputs N -element measured photon count vectors under a chosen noise model, \tilde{y} . The classifier is a single-layer network that takes \tilde{y} as input and outputs \tilde{x} , also an N -element vector. The objective is to minimize the MSE between the input images and the output vectors, $\|\tilde{x} - x\|_2^2$. In noiseless cases, the classifier is equivalent to M^{-1} , where M is the masks used in the scanner.

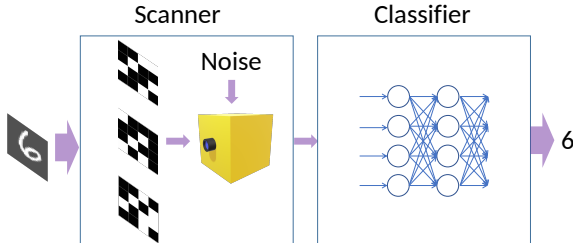


Figure 2: Model configuration

ONN Optimization under Poisson Noise. Optimizing the scanner can be challenging as the Poisson noise generating function typically lacks a gradient. While reparameterization is a useful method for addressing AGN, it is not as effective for addressing Poisson noise. To address this limitation, we employ a method mentioned by Cossairt et al. that utilizes a normal distribution with a variance equal to its expectation to approximate the Poisson distribution during training [3]. This approximation enables us to employ PyTorch built-in reparameterization method, i.e. `rsample`, and optimize the scanner more effectively under Poisson noise.

To approximate the Poisson noise by the AGN, we can re-write the measurement with noise $\tilde{\mathbf{y}} = \mathbf{M}\mathbf{x} + \mathbf{J}$ where $\mathbf{J} = (\mathbf{M}\mathbf{x})^{\frac{1}{2}} \odot \boldsymbol{\epsilon}$, $\boldsymbol{\epsilon} \sim \mathcal{N}(0, \mathbf{I})$. During the training under Poisson noise, \mathbf{J} also plays a role in gradient computation, which is the most significant difference compared with training under the AGN.

4.2. Sensing Matrices by Priors

In the preceding section, we discussed the generation of masks M using different coding strategies. Evaluating the efficacy of these strategies for a given scenario requires a systematic assessment of their respective priors. Image priors come in varying types and can enhance model robustness in noisy environments and improve overall image quality [3], [29]. It is important to note that all the strategies outlined in this paper possess three distinct prior levels.

- **Null prior** (data is not compressible or needs to be reconstructed without priors). Coding strategies in this category require no information about the data. They usually generate full rank matrices as M . In this project, we chose Raster Scan (RS), Binary Random Basis (BR), and Hadamard Basis (HB) for performance evaluation. M for RS is an identity matrix while it is a Hadamard matrix for HB. BR employs random values for each pixel in the mask, i.e $M \in \{0, 1\}^{N \times N}$. On top of these strategies, we also include Impulse Imaging (II) which works as a golden standard in this project. II is an ideal case assuming it can capture the whole data spectrum simultaneously. Mathematically, the sensing matrix M of II is also an identity matrix, but each mask in II has N times longer exposure time compared with RS.
- **Reconstruction prior** (data is moderately compressible). One common strategy in coding for images

is to take advantage of the fact that noise tends to have a greater impact on high-frequency components. To investigate this phenomenon, we utilized a Low-Frequency-Hadamard Basis approach, in which only the low-frequency vectors of a Hadamard matrix are retained. This approach is referred to as Truncated Hadamard (TH) in this paper.

- **Task-Specific prior or Selective Sensing prior** (data is extremely compressible). Coding strategies are an essential component of signal processing that involve gathering task-specific information from data. In order to design these strategies, sensing matrices M are developed, which can vary depending on the task at hand. One such approach is the Hardware Principal Components Analysis (PCA) technique, which identifies the most principal components in the training data and uses them to construct masks. Another strategy uses a sensing matrix M that is not pre-defined or fixed, but rather is optimized using a Neural Networks model during training. In this project, this optimization method is referred to as Optical Neural Networks (ONN).

In this study, we examine the impact of various priors on a single-pixel imaging system in terms of classification. Firstly, we explain our methods for implementing constraints in the single-pixel imaging model. Then, we simulate the effect of different prior types on classification performance using the MNIST dataset. Finally, we test the feasibility of these strategies through experiments.

4.3. Constraints Implementation

In this section, we outline our methods for implementing the model optically. In order to ensure that our model is valid, we have implemented techniques that satisfy both the Flux-preserving and Positivity-preserving constraints. By using these techniques, we can ensure that the model accurately represents the underlying physical processes and produces results that are both reliable and interpretable.

4.3.1. Photon Distribution Factor. Optimizing M subject to constraint 1 can be challenging. To overcome this limitation, we propose the use of a scale factor, known as the Photon Distribution Factor λ , which allows us to select any values for M without violating constraint 1. The Photon Distribution Factor is calculated as

$$\lambda = \frac{\rho\tau}{N \sum_{k=1}^m v_k} \quad (4)$$

, where ρ is the number of photons per second projected onto the DMD, τ is the total exposure time for all masks, N is the number of pixels, and v_k is the greatest value of the k^{th} mask. The maximum value v_k is chosen as its corresponding pixel is open for longer than any other pixel in the k^{th} mask, and the exposure time of this mask depends solely on v_k . Moreover, the total exposure time τ is proportional to $\sum_{k=1}^m v_k$, while the total number of photons from the field of view is $\tau \sum_{i=1}^N \frac{\rho}{N} x_i$.

By utilizing the Photon Distribution Factor, we can guarantee that constraint 1 is never violated. With this in mind, we can re-formulate the model in Equation 1 into the following equation,

$$\tilde{y} = \frac{1}{\lambda} f_r(\lambda Mx) \quad (5)$$

Here, f_r generates random numbers with an expected value of λMx to simulate noise and produce a measurement with noise, denoted as \tilde{y} .

4.3.2. Dual-Rail Technique for Negative Entries. To satisfy constraint 2, the dual-rail technique [27] employs two complementary measurement branches: one measures with all positive entries, denoted as M^+ , while the other measures with all negative entries, denoted as M^- . By doing so, the dual-rail technique effectively converts the constraint on negative entries to a constraint on the difference between the measurements made by the two branches.

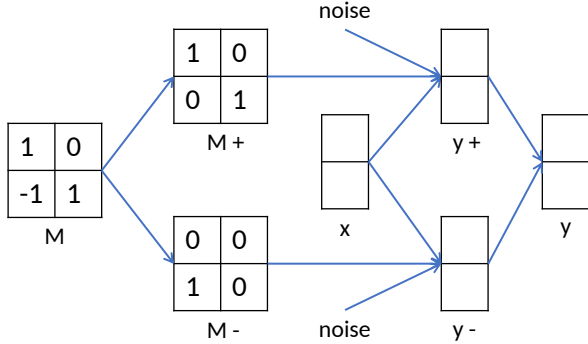


Figure 3: Dual-Rail technique

To implement the two branches, we split the mask M into two components: $M^+ = \max(M, 0)$ and $M^- = \max(-M, 0)$, with the superscripts indicating the respective branches. This enables us to express $\lambda\tilde{y}$ as the difference between the photon counts with noise measured by M^+ and M^- , denoted $\lambda\tilde{y}^+$ and $\lambda\tilde{y}^-$, respectively. Notably, the two-rail approach also modifies the expression for the Photon Distribution Factor. In the case that each branch has a PMT,

$$\lambda = \frac{\rho\tau}{N \sum_{k=1}^m |v_k|} \quad (6)$$

, where $|\cdot|$ takes the absolute value. In the case of using only one PMT, it is worth noting that the Photon Distribution Factor changes to

$$\lambda = \frac{\rho\tau}{N(\sum_{k=1}^m v_k^+ + \sum_{k=1}^m v_k^-)} \quad (7)$$

, since one PMT measures with both M_k^+ and M_k^- sequentially to obtain the measurement result for M_k . All the parameters in this updated Photon Distribution Factor are of the same meaning as in section 4.3.1, and v_k^+ and v_k^- stand for the maximum values of M^+ and M^- respectively.

4.4. Simulations

4.4.1. MNIST Data Pre-processing. The MNIST dataset, which comprises handwritten digits ranging from 0 to 9, has a default size of 28 by 28 pixels [30]. To align the data with Hadamard matrices, we added black pixels to the edges of the images and resized them to 32 by 32 pixels [30]. Subsequently, we rescaled the pixel values from the original range of $[0, 1]$ to $[0.3, 1]$. This rescaling was aimed at improving the dataset's suitability for different noise models, as the initial black backgrounds do not introduce Poisson noise, which is typically proportional to the expected photon counts.

4.4.2. Performance Evaluation. The model performances were assessed based on their average classification rates, which were calculated after five independent tests. In each test, the dataset was randomly split into 70% for training and 30% for validation. The model generated noisy photon counts during each assessment, and the training continued until the validation rate reached a plateau or declined. The highest validation rate obtained during the training process was considered as the representative upper bound for each assessment. The overall model performance was determined by averaging the results from all five assessments. This comprehensive evaluation ensured the reliability and accuracy of the model performance.

4.5. Experiments

To further support our conclusions, we conducted an experiment in addition to simulations. The experiment utilized a DMD (digital micromirror device), specifically the DLP 7000 model from Texas Instruments, and a PMT (photomultiplier tube) from PicoQuant, specifically the PMA Series. The experimental setup involved both hardware-end data acquisition and software-end classifier training.

To ensure that the classifier was accurately trained using the PMT data, we performed a transformation and re-calibration of the MNIST images to match what the PMT would actually "observe" during data acquisition. This step is crucial when training the classifier without the use of hardware-end data. By implementing this transformation and re-calibration process, we were able to accurately simulate the imaging conditions that the PMT would encounter during actual data acquisition, allowing for more reliable and robust classification results.

First, we performed a Raster scan of a sample from the MNIST dataset, with each mask exposed for 1 second. The light intensity was adjusted to ensure that the brightest pixel generated approximately 1000 photon counts per second. The data captured during this experiment was then reshaped into a 32 by 32 image, which can be regarded as a linearly transformed version of the original raw image.

Then, we estimated the linear transformation between the digital and experimental data to ensure that the digital data closely matched the sensor's observations. After applying this transformation to all digital data, we used it to train

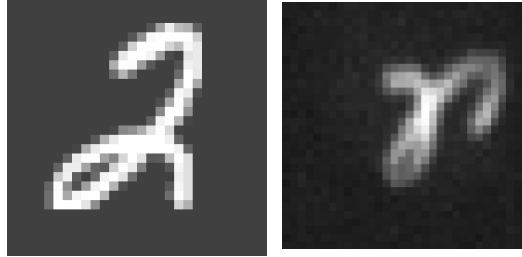


Figure 4: Raw image (left) VS measured image

the software-end classifier through simulation. Additionally, in this step, the masks used for Selective Sensing were also trained. The masks with decimals use the fraction of a super pixel [22] The ONN training is called *in silico* method (Wright et al) [22], [31]

After generating the mask pattern sequences, we uploaded them onto the DMD to acquire the data, denoted as \hat{y} . Our test set consisted of ten handwritten images, each of which appeared exactly once during the experiment. To control the noise level in the data, we varied lengths of random intervals throughout the 1-second exposure time for each mask. By preserving the arrival times of all photons, we were able to systematically adjust the level of noise in the acquired data.

5. Results

5.1. Mask optimization with ONN

The primary question to address is whether the ONN has the ability to identify noise specific optimized masks. We established a benchmark by comparing the reconstruction performance in terms of mean squared error (MSE) between the original and reconstructed images, denoted by $\|\tilde{x} - x\|_2^2$, where $\tilde{x} = M^{-1}\hat{y}$. The reconstructed images were obtained using the Hadamard basis and Raster basis under Poisson noise and AGN models respectively. The outcomes, depicted in Figure 5 where the x-axis is the log-scaled MSE of impulse imaging with different exposure times, indicate that the Hadamard basis is less effective in the presence of Poisson noise, while it is more effective under the AGN model when compared to the Raster basis. Given that many algorithms rely on the AGN model, their conclusions may not hold if the optimal masks differ under Poisson noise.

To make this reconstruction task less specific and more general, we reshaped the input data vectors x from 10^5 random 8 by 8 patterns, increasing their generality. We randomly re-generated x in different training epochs, introducing additional variability. The simulations were conducted under significant noise, with a total of 1×10^3 photons. We initialized the masks M with an $N \times N$ identical matrix and optimized them until the model reported constant losses.

Figure 6 displays the first 6 optimized masks generated by the ONN model. A notable observation is that the model exhibits distinct behavior patterns under the AGN and

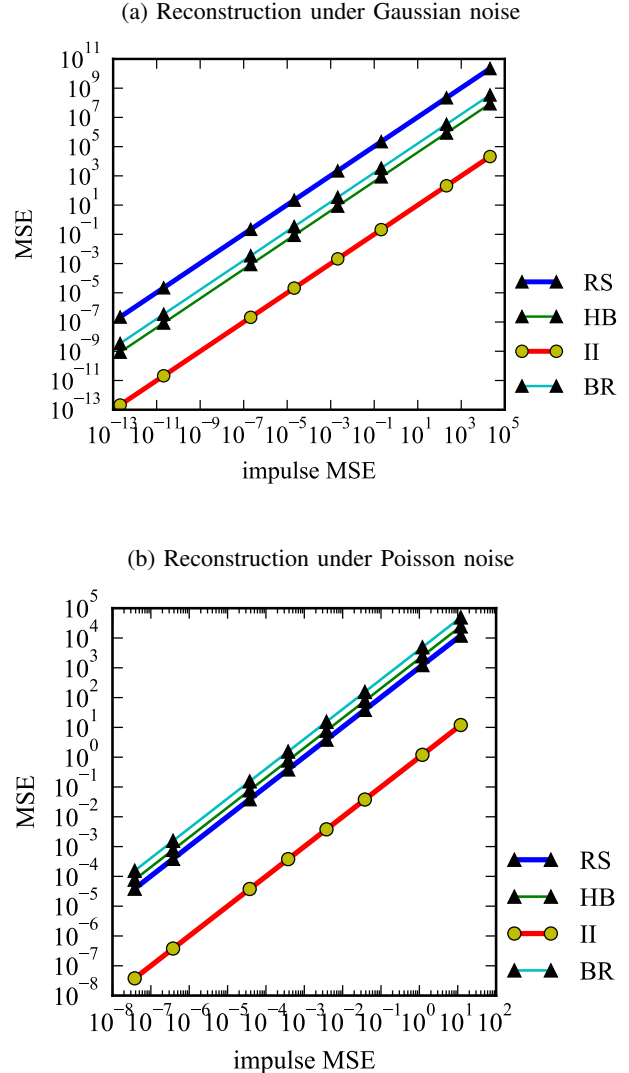
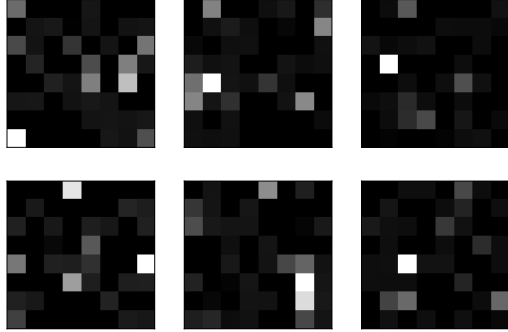


Figure 5: Reconstruction errors on simulated data. RS: Raster basis. HB: Hadamard basis. II: Impulse imaging. BR: Binary random basis. (a) RS is always worse than HB for all noise levels under Gaussian noise. (a) HB is no better than RS under Poisson noise.

Poisson noise. Specifically, it tends to open more pixels to enhance light throughput under the AGN, but adheres to the RS mode under the Poisson noise. Figure 7 provides a more detailed visualization of the optimized masks by presenting the distribution of their entries. The x-axis represents the values in the masks, while the y-axis shows the total number of entries within a specific range. This observation aligns with the reconstruction results, where the RS performed modestly under the AGN but considerably better under the Poisson noise. The rationale behind this is that re-projection from a captured basis into a basis of sparsity does not yield the same recovery quality under Poisson noise that

is provides for AGN. To obtain a performance benefit over the trivial point scanning method, or RS, it is essential that the data is sparse and is captured in a sparse basis. Since random patterns are not sparse, the best scanning strategy is the point scanning, which matches our results.

(a) Optimal masks under Gaussian noise



(b) Optimal masks under Poisson noise

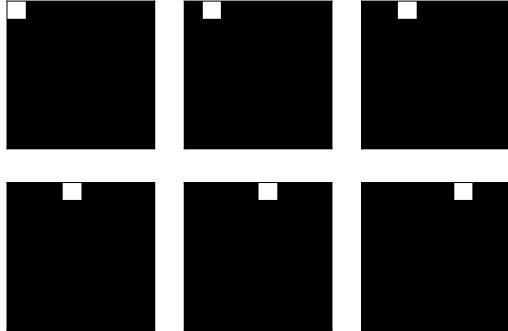


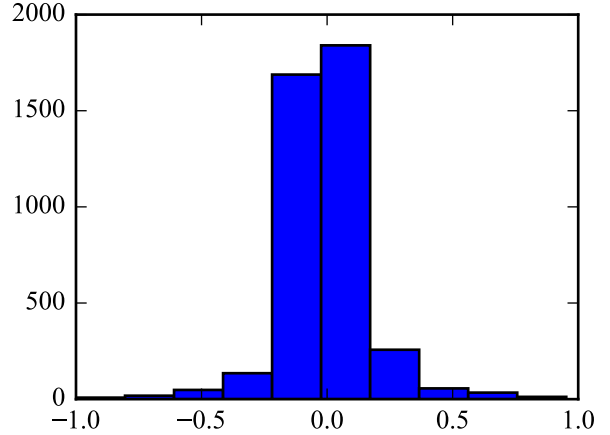
Figure 6: First 6 optimized masks

The results from optimizing the masks indicate that the optimal masks under the AGN model may not perform similarly under Poisson noise. Specifically, methods developed under the AGN assumption may not be effective when the measured data follows a Poisson distribution. The inherent differences in the underlying noise models of the two distributions can lead to suboptimal performance of AGN-optimized masks in Poisson noise scenarios. Therefore, it is crucial to consider Poisson noise when designing coding schemes and algorithms for imaging applications, especially when working with state-of-the-art sensors.

5.2. Classification Rates on Simulated Data

We evaluated our proposed model through simulations that tested both AGN and Poisson noise models, using

(a) Value distribution of the optimal masks under Gaussian noise



(b) Value distribution of the optimal masks under Poisson noise

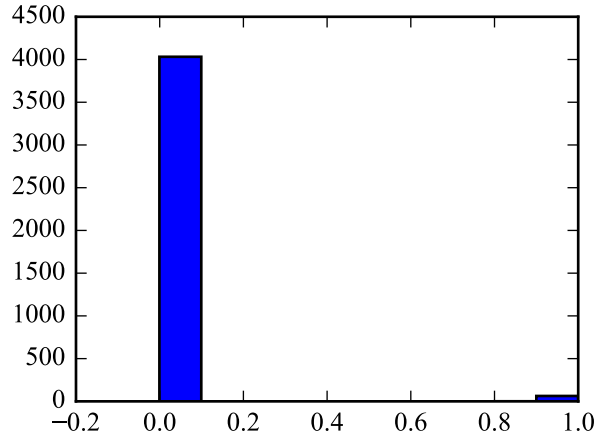


Figure 7: Masks values distribution. (a) Given a Raster scan mask family, ONN returns a different mask family under the AGN, indicating that Raster scan is always suboptimal. (b) ONN adheres to the Raster scan, suggesting it is optimal under Poisson noise.

varying exposure times to generate results at different noise levels. We also tested all compressible strategies, varying the total number of masks, and defined a metric called compression ratio as the ratio of the number of masks to the number of pixels [32]. For RS and HB, this ratio was constrained to be 1.00, while the rest were evaluated over values in $\mathcal{C}_R = \{0.01, 0.04, 0.09, 0.16, 0.25, 0.36, 0.49, 0.64, 0.81, 1.00\}$. Unlike pre-defined masks used by other strategies, the initial masks for ONN can affect performance in the presence of noise. We therefore initialized its masks with the PCA components from the training data, which typically yield better performance.

Figure 8 displays the classification performance of different parameters. The x-axis is the log-scaled mean square error (MSE) of impulse imaging (II) with varying exposure times. This MSE is the gold standard in this project and serves as a metric to measure the noise level for both AGN and Poisson noise models. The y-axis represents the validation set's classification rate. We explored all the values in \mathcal{C}_R to determine the best compression ratio for TH, PCA, and ONN since compression ratio affects classification performance. The figure shows the best results among all compression ratios for each strategy.

The results presented in the figure demonstrate that II consistently achieves the highest performance, which is in line with our expectations. In the presence of AGN, all coding schemes exhibit significant improvements over RS and in many cases provide adequate performance. This is because under Gaussian noise, projected from a captured basis into a basis of sparsity where the classifier operates can be done without a significant noise penalty. Moreover, for the classification task at hand, low-rank measurement techniques such as HB, PCA, and ONN, can yield further improvements in classification performance. Notably, the ONN approach produces results that are nearly as good as the II approach, while using only 0.1% of the photons.

However, when dealing with Poisson-distributed measured data, the effectiveness of Hadamard-based (HB) coding is no longer superior to that of RS. This aligns with the findings of Harwit et al. [7], which discourage the adoption of coding for Poisson noise. Despite this, there is still potential for performance improvement by utilizing low-rank methods such as TH, PCA and ONN. This is likely due to the fact that the images with analyze do in fact have sparsity in the Hadamard basis. Selective Sensing where capture patterns are optimized to capture sparsity directly like the ONN can retain their performance under poisson noise making them viable replacements for simple point scanners. This indicates that Selective Sensing is the most optimal approach for both noise models.

5.3. Classification Performances on Experiment Data

In our experiments, we utilized a DMD and a PMT to measure ten handwritten digits from the MNIST dataset. To train the models, we employed 10^5 photons, which constituted a higher noise level in comparison to the experimental setup. The collected data took the form of a series of timestamps recording the photons' arrival time. During data collection, both RS and HB used 1024 masks, while the TH and HB employed the same measured data, but the TH used only the first 92 measurements. Similarly, PCA and ONN utilized 92 masks. Physical measurements took one second per mask for all strategies. To generate data with higher noise levels from the raw data, we randomly selected intervals within the 1-second span and counted the total number of photons within them. Since the ONN and PCA had only 92 masks, the maximum exposure time was set to 92 seconds. To ensure a fair comparison, we computed

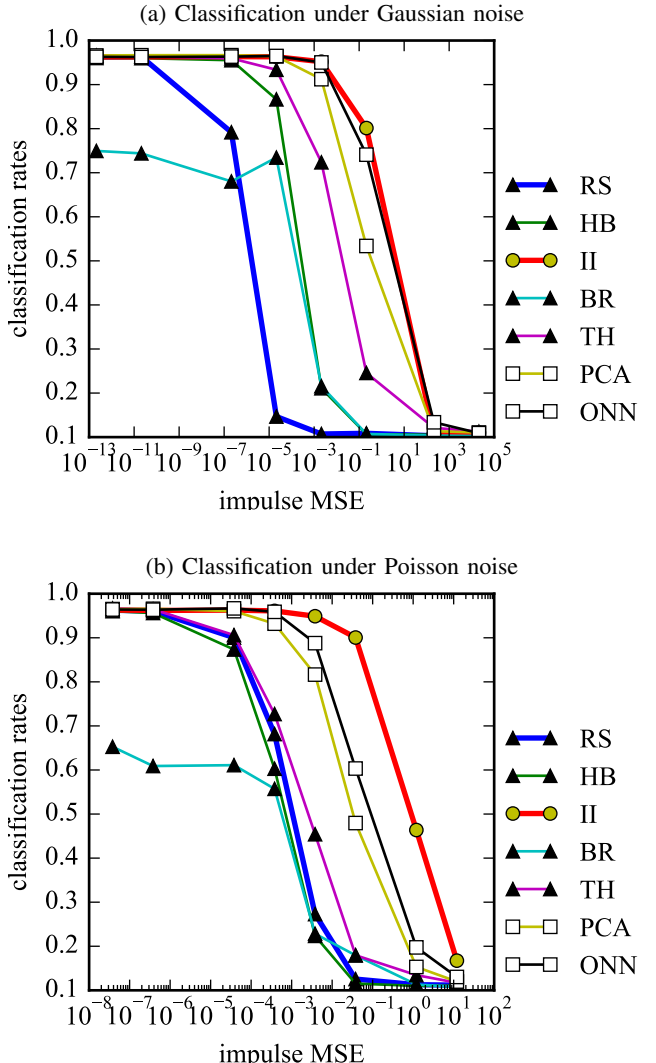


Figure 8: Classification rates on simulated data. RS: Raster basis. HB: Hadamard basis. II: Impulse imaging. BR: Binary random basis. TH: Truncated Hadamard basis. PCA: PCA basis. ONN: Optical Neural Networks. Selective strategies are marked by \square and non-selective strategies are marked by \blacktriangle . (a) RS is the worst but using other non-selective coding strategies can improve the performance under the AGN. (b) All non-selective strategies Only selective strategies can improve the performance under Poisson noise.

the interval length for each strategy as $\frac{\tau}{m}$, where τ represents the total exposure time under investigation, and m denotes the number of masks used for each strategy.

Figure 9 displays the classification rates achieved on the experimental data. The x-axis shows the exposure time, and the y-axis represents the classification rates of the models. Although there may be discrepancies between software training and hardware data acquisition, the ONN models performed excellently. However, the figure reveals some un-

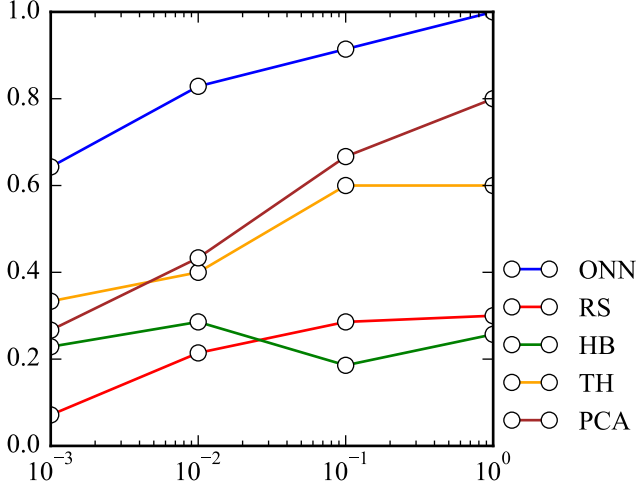


Figure 9: Classification rates on experiment data. RS: Raster basis. HB: Hadamard basis. TH: Truncated Hadamard basis. PCA: PCA basis. ONN: Optical Neural Networks. ONN is in general the best strategies given the experimental data.

expected phenomena. Firstly, the HB strategy outperformed the RS for short exposure times, which was not observed in the simulations. This phenomenon may have arisen due to the dark photon in the PMT, a signal-independent noise that has about 40-80 counts per second, and was more pronounced in short exposures. Secondly, the TH achieved better classification performances than the PCA when the exposure time was short. This result was due to the use of unneeded PCA masks. To verify, we conducted simulations and made figure 10 by fixing the total number of photons at 10^5 and varying the compression ratio under the Poisson noise. This figure showed that the PCA method could perform worse than the TH if extra masks were used. Hence, the PCA strategy requires careful estimation of the noise level to avoid using extra masks. Notably, the ONN appeared more stable when including extra masks, which is another advantage of the ONN. The ONN can perform robustly even with suboptimal numbers of masks, unlike the PCA strategy, which is noise-level sensitive. While it is possible to set the noise level during training, the effectiveness of the ONN can be evaluated for other levels of noise as well. This flexibility in application allows for broader use of the ONN beyond its specific training conditions, increasing its potential impact and utility in real-world scenarios.

5.4. Experiment on Hyper-Spectral Dataset

For this experiment, we use the Indian Pines dataset [33], which was acquired by employing Airborne Visible / Infrared Imaging Spectrometer (AVIRIS) on June 12, 1992 over the Purdue University Agronomy farm northwest of West Lafayette and the surrounding area. This dataset is composed of 145×145 pixels and 224 spectral reflectance bands in the wavelength range 0.4 to $2.5 \mu\text{m}$. In Figure 11, the classes of the Indian Pines dataset are depicted, along

with the respective counts within the dataset. The figure showcases an illustration of one channel (band 12) for all pixels, along with the ground truth of semantic labeling.

In this experiment, we zero-padded each spectrum from 224 to 256 to align with the Hadamard mask. Spectral data are normalized within the range of $[0, 1]$. The scanner-classifier module from figure 2 was utilized, with modifications made to the ONN classification layers to match the sizes of the new dataset. Each classification was performed for 2000 epochs, with a learning rate of 5×10^{-3} and batch size of 5000. Figure 13 shows the classification rates for the Indian Pines dataset varying light level from 10^1 to 10^{10} .

6. Discussion and Limitations

This paper highlights the challenges of computational imaging under Poisson noise and its impact on algorithms based on the AGN noise assumption. We find that for compressible measurements, and especially tasks that involve direct feature extraction instead of signal reconstruction, a Selective Sensing approach using task optimized codes provides a viable coding solution. Through simulations and experiments, we demonstrate the feasibility of Selective Sensing and its promising classification performance on the MNIST handwritten number dataset. It is also robust in application scenarios with difficult-to-estimate noise levels. Our ONN method represents a method that can generate these selective measurements. Furthermore, Selective Sensing motivates the development of optical ANNs or ANNs with optical layers to globally optimize imaging systems.

Despite the promising results of our project, there are some limitations that must be acknowledged. First, we used a Gaussian noise model with reparameterization to train our model, which is only an approximation of the actual quantization noise at the sensor. Second, our test set consisted of only 10 numbers, which may not provide a comprehensive evaluation of the model's performance. Additionally, we noted an inconsistency in that the model was trained using simulated data but tested with experimental data. Lastly, the Photon Distribution Factor rescales the masks M , but its value changes during training and is not evolved during back-propagation. These limitations highlight the need for further improvements in the optimization of the ONN model, such as using more advanced optimization methods and larger sets of experimental data. Our work highlights the importance of the integration of imaging hardware and signal processing. In single photon accurate imaging systems, comprehensibility and sparsity of the data can be exploited to far greater effect during the measurement, as opposed to post processing.

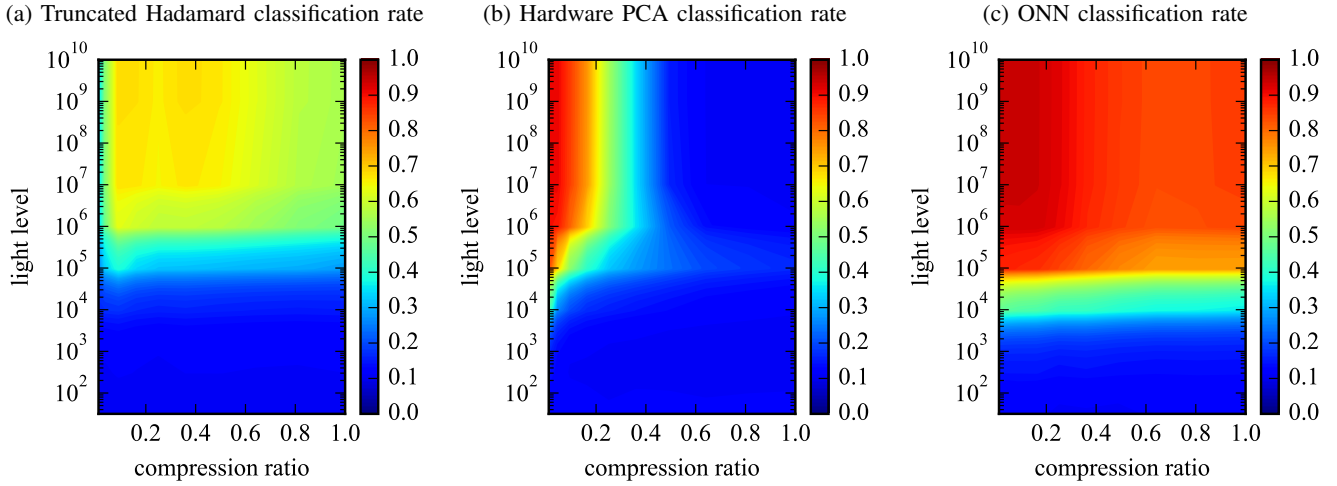


Figure 10: Classification rates on simulated data w.r.t compression ratios and light levels. The models were trained using a light level of 10^5 and subsequently tested under different light levels. It was observed that hardware PCA performance deteriorates when the compression ratio is not properly chosen, whereas the Truncated Hadamard and ONN models exhibit greater robustness in such scenarios.

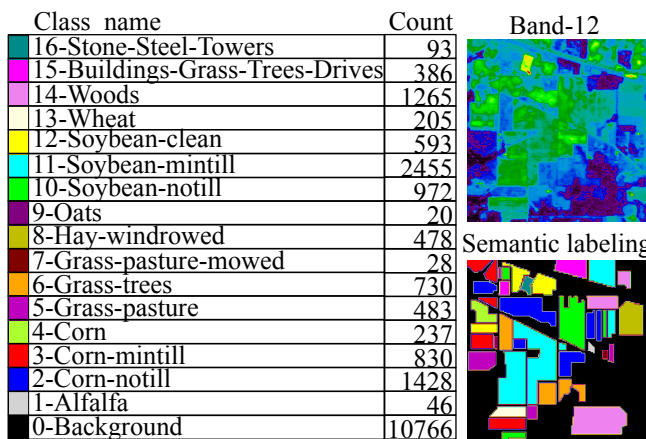


Figure 11: Indian Pines dataset [33]

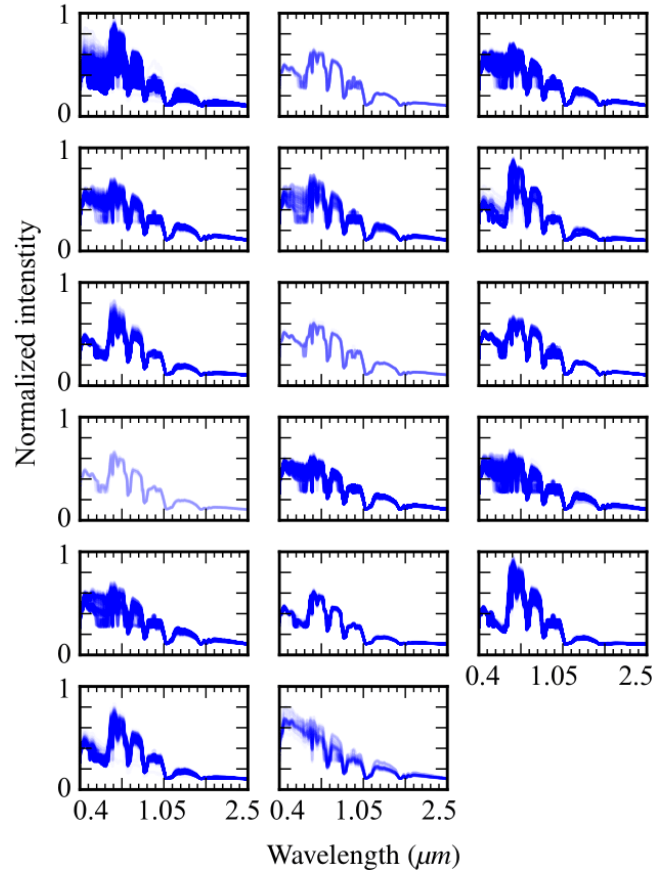


Figure 12: Spectrum for each class in the Indian Pines dataset

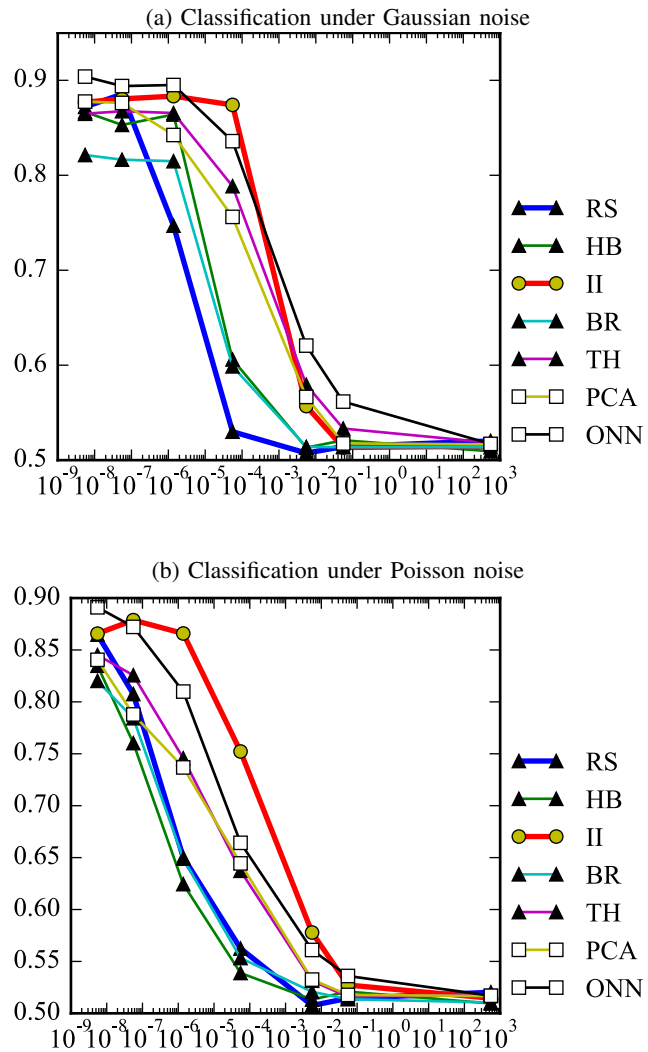


Figure 13: Classification rates of Indian Pines dataset varying light level. RS: Raster basis. HB: Hadamard basis. II: Impulse imaging. BR: Binary random basis. TH: Truncated Hadamard basis. PCA: PCA basis. ONN: Optical Neural Networks.

References

- [1] M. Raginsky, R. M. Willett, Z. T. Harmany, and R. F. Marcia, “Compressed sensing performance bounds under poisson noise,” *IEEE Transactions on Signal Processing*, vol. 58, no. 8, pp. 3990–4002, 2010.
- [2] R. Raskar, “Computational photography: Epsilon to coded photography,” in *Emerging Trends in Visual Computing: LIX Fall Colloquium, ETVC 2008, Palaiseau, France, November 18-20, 2008. Revised Invited Papers*. Springer, 2009, pp. 238–253.
- [3] O. Cossairt, M. Gupta, and S. K. Nayar, “When does computational imaging improve performance?” *IEEE Transactions on Image Processing*, vol. 8, no. 2, pp. 70 773–70 783, 2013.
- [4] R. Foord, R. Jones, C. Oliver, and E. Pike, “The use of photomultiplier tubes for photon counting,” *Applied optics*, vol. 8, no. 10, pp. 1975–1989, 1969.
- [5] J. Prescott, “A statistical model for photomultiplier single-electron statistics,” *Nuclear Instruments and Methods*, vol. 39, no. 1, pp. 173–179, 1966. [Online]. Available: <https://www.sciencedirect.com/science/article/pii/0029554X66900590>
- [6] F. J. Lombard and F. Martin, “Statistics of electron multiplication,” *Review of Scientific Instruments*, vol. 32, no. 2, pp. 200–201, 1961.
- [7] M. Harwit and N. J. A. Sloane, *Hadamard Transform Optics*. Academic Press, 1979.
- [8] R. D. Swift, R. B. Wattson, J. A. Decker, R. Paganetti, and M. Harwit, “Hadamard transform imager and imaging spectrometer,” *Applied optics*, vol. 15, no. 6, pp. 1595–1609, 1976.
- [9] C. Scotté, F. Galland, and H. Rigneault, “Photon-noise: Is a single-pixel camera better than point scanning? a signal-to-noise ratio analysis for hadamard and cosine positive modulation,” *arXiv preprint arXiv:2210.01915*, 2022.
- [10] A. Wuttig, “Optimal transformations for optical multiplex measurements in the presence of photon noise,” *Appl. Opt.*, vol. 44, no. 14, pp. 2710–2719, May 2005. [Online]. Available: <https://opg.optica.org/ao/abstract.cfm?URI=ao-44-14-2710>
- [11] L. W. Schumann and T. S. Lomheim, “Infrared hyperspectral imaging fourier transform and dispersive spectrometers: comparison of signal-to-noise-based performance,” in *Imaging Spectrometry VII*, vol. 4480. SPIE, 2002, pp. 1–14.
- [12] N. Larson, R. Crosmun, and Y. Talmi, “Theoretical comparison of singly multiplexed hadamard transform spectrometers and scanning spectrometers,” *Applied optics*, vol. 13, no. 11, pp. 2662–2668, 1974.
- [13] L. Streeter, G. Burling-Claridge, M. Cree, and R. Künnemeyer, “Optical full hadamard matrix multiplexing and noise effects,” *Applied Optics*, vol. 48, no. 11, pp. 2078–2085, 2009.
- [14] R. Willett and M. Raginsky, “Poisson compressed sensing.”
- [15] S. Diamond, V. Sitzmann, F. Julca-Aguilar, S. Boyd, G. Wetzstein, and F. Heide, “Dirty pixels: Towards end-to-end image processing and perception,” *ACM Transactions on Graphics (TOG)*, vol. 40, no. 3, pp. 1–15, 2021.
- [16] K. Zhang, J. Hu, and W. Yang, “Deep compressed imaging via optimized pattern scanning,” *Photonics research*, vol. 9, no. 3, pp. B57–B70, 2021.
- [17] C. Hinojosa, J. C. Niebles, and H. Arguello, “Learning privacy-preserving optics for human pose estimation,” in *Proceedings of the IEEE/CVF international conference on computer vision*, 2021, pp. 2573–2582.
- [18] X. Dun, H. Ikoma, G. Wetzstein, Z. Wang, X. Cheng, and Y. Peng, “Learned rotationally symmetric diffractive achromat for full-spectrum computational imaging,” *Optica*, vol. 7, no. 8, pp. 913–922, 2020.
- [19] C. A. Metzler, H. Ikoma, Y. Peng, and G. Wetzstein, “Deep optics for single-shot high-dynamic-range imaging,” in *Proceedings of the IEEE/CVF Conference on Computer Vision and Pattern Recognition*, 2020, pp. 1375–1385.
- [20] J. Chang and G. Wetzstein, “Deep optics for monocular depth estimation and 3d object detection,” in *Proceedings of the IEEE/CVF International Conference on Computer Vision*, 2019, pp. 10 193–10 202.
- [21] E. Onzon, F. Mannan, and F. Heide, “Neural auto-exposure for high-dynamic range object detection,” in *Proceedings of the IEEE/CVF conference on computer vision and pattern recognition*, 2021, pp. 7710–7720.
- [22] J. Spall, X. Guo, and A. I. Lvovsky, “Hybrid training of optical neural networks,” *Optica*, vol. 9, no. 7, pp. 803–811, Jul 2022. [Online]. Available: <https://opg.optica.org/optica/abstract.cfm?URI=optica-9-7-803>
- [23] E. Tseng, A. Mosleh, F. Mannan, K. St-Arnaud, A. Sharma, Y. Peng, A. Braun, D. Nowrouzezahrai, J.-F. Lalonde, and F. Heide, “Differentiable compound optics and processing pipeline optimization for end-to-end camera design,” *ACM Transactions on Graphics (TOG)*, vol. 40, no. 2, pp. 1–19, 2021.
- [24] J. D. Rego, H. Chen, S. Li, J. Gu, and S. Jayasuriya, “Deep camera obscura: an image restoration pipeline for pinhole photography,” *Optics Express*, vol. 30, no. 15, pp. 27 214–27 235, 2022.
- [25] M. F. Duarte, M. A. Davenport, D. Takhar, J. N. Laska, T. Sun, K. F. Kelly, and R. G. Baraniuk, “Single-pixel imaging via compressive sampling,” *IEEE Signal Processing Magazine*, vol. 25, no. 2, pp. 83–91, 2008.
- [26] T. Wang, S.-Y. Ma, L. G. Wright, T. Onodera, B. C. Richard, and P. L. McMahon, “An optical neural network using less than 1 photon per multiplication,” *Nature Communications*, vol. 13, no. 1, p. 123, 2022.
- [27] H. S. Pal and M. A. Neifeld, “Multispectral principal component imaging,” *Opt Express*, vol. 11, no. 18, pp. 2118–25, 2003 Sep 8.
- [28] A. K. Boyat and B. K. Joshi, “A review paper: Noise models in digital image processing,” *ArXiv*, vol. abs/1505.03489, 2015.
- [29] A. Levin, R. Fergus, F. Durand, and W. T. Freeman, “Image and depth from a conventional camera with a coded aperture,” *SIGGRAPH*, 2007.
- [30] Y. Lecun, L. Bottou, Y. Bengio, and P. Haffner, “Gradient-based learning applied to document recognition,” *Proceedings of the IEEE*, vol. 86, no. 11, pp. 2278–2324, 1998.
- [31] G. Wright, T. Onodera, M. Stein, T. Wang, D. Schachter, Z. Hu, and P. McMahon, “Deep physical neural networks enabled by a backpropagation algorithm for arbitrary physical systems (2021),” URL: <https://arxiv.org/abs/2104.13386>.
- [32] R. Stojek, A. Pastuszczak, P. Wróbel, and R. Kotyński, “Single pixel imaging at high pixel resolutions,” *Optics Express*, vol. 30, no. 13, pp. 22 730–22 745, 2022.
- [33] M. F. Baumgardner, L. L. Biehl, and D. A. Landgrebe, “220 band aviris hyperspectral image data set: June 12, 1992 indian pine test site 3,” Sep 2015. [Online]. Available: <https://purr.purdue.edu/publications/1947/1>

Acknowledgments

The authors would like to thank...